# A Modified Model for Specular Sea Surface Emissivity at Microwave Frequencies

Sandra L. Cruz-Pol and Christopher S. Ruf, *Senior Member, IEEE*

***Abstract*—Modifications to the [14] model for specular ocean emissivity have recently been suggested by [7] in order to improve the performance at high microwave frequencies. The work presented here tests both the original and modified models using a set of satellite and ground-based observations that is designed to eliminate as much as possible the dependence of the test on parameters other than the surface emission itself. Clear sky, low humidity, and low wind conditions were used exclusively to reduce the dependence of the test on atmospheric and wind-roughened sea models. Radiosonde observations (RaObs) coincident with TOPEX satellite overpasses were used to reduce errors due to inexact knowledge of the atmosphere. Our tests confirm the superior performance of the Ellison model at higher frequencies. In an effort to remove the residual bias between the models and the observations, we also suggest a parameterized modification to both models that "best fits" the models to the data. In this case, the modified Ellison model maintains its superior performance at high frequencies, suggesting that it has an inherently more accurate frequency dependence. The root mean-squared (RMS) error in the modified Ellison emissivity model, over the range of 18–40 GHz, is found to be 0.0037, which translates into a model error of approximately 1 K in terms of brightness temperatures.**

***Index Terms*—Microwave remote sensing, ocean emissivity.**

## I. Introduction

THE need to improve the calibration of existing models for thermal emission by the ocean is motivated by several current and upcoming satellite remote sensing missions. Possible discrepancies between one standard model for specular ocean surface emission (as described in [14]) and satellite observations have been noted by numerous investigators (e.g., [30], [20], [9]). In each of these cases, comparisons between the [14] model (henceforth referred to as KS77) and observations have been made at microwave frequencies well above the original intended frequency range of the model. Recent work by [17] has attempted to update the KS77 model using laboratory measurements of the permittivity of ocean water samples at a wider range of frequencies. Validation of this updated model (henceforth referred to as E96) was presented in both [7] and [9]. In both cases, the validation consisted of comparisons between satellite observations and modeled brightness temperatures ($T_B$). Both studies found that E96 agreed more closely with the measurements than did KS77. However, in addition to a model for specular ocean surface emission, the complete $T_B$ model used in these validation studies required corrections for surface winds and atmospheric absorption. One possible limitation with the studies was the degree to which their $T_B$ models were compromised by inexact knowledge of the surface winds and atmospheric conditions, as well as by possible errors in the models for wind-induced excess emissivity and atmospheric absorption.

[7] compared their model with Topex Microwave Radiometer (TMR) data from the North Atlantic during 5 1/2 weeks in the Fall of 1993. They modeled the wind-roughened sea and the atmosphere using the European Center for Medium Range Weather Forecast (ECMWF) model predictions of 10-m winds and atmospheric profiles. The ECMWF uses ship and buoy measurements to generate a meteorological prediction every 6 h. Its accuracy for monitoring water vapor variations in the atmosphere is approximately 9% for humid atmospheric conditions and lower for dry conditions [26]. They used the oxygen and water vapor atmospheric-absorption model by [15]. [9] uses TMR as well as SSM/I and ERS-1 ATSR/M observations but also relies on ECMWF meteorological fields for their wind and atmosphere corrections.

We present here another comparison study between TOPEX satellite observations and both the KS77 and E96 surface models, in which we have attempted to reduce as much as possible the sensitivity to both wind and atmospheric corrections. We employ colocated TOPEX altimeter data to select only low wind conditions in order to reduce the dependence of our analysis of the accuracy of the wind model. Coincident RaOb profiles of the atmosphere are used during TOPEX overpasses of island launch sites to more accurately account for the atmosphere. Furthermore, our comparison is limited to low humidity conditions only (path delay <15 cm) in order to reduce the dependence of our analysis on the accuracy of the atmospheric model. Finally, we consider an improved atmospheric absorption model, as described in [4].

Our results confirm those in [7] and [9], that the E96 model is more accurate at the higher microwave frequencies. In addition, our intercomparison database is used to modify both models to "best fit" the data. In this case, the inherent frequency dependence of the modified E96 model is still superior to that of the modified KS77.

Our model for the brightness temperature measured by a downward-looking spaceborne microwave radiometer has three components. The radiometer measures the upwelling emission from the atmosphere, the emission by the surface, and the downwelling emission reflected at the surface. The total

Manuscript received September 21, 1998; revised July 16, 1999.

S. L. Cruz-Pol is with the Department of Electrical and Computer Engineering, University of Puerto Rico, Mayagüez, PR.

C. S. Ruf is with the Department of Electrical Engineering, The Pennsylvania State University, University Park, PA 16802 USA.

Publisher Item Identifier S 0196-2892(00)01053-6.

brightness temperature in the zenith direction is given by (e.g., [27])

$$T_a = T_{UP} + \epsilon_s T_s e^{-\tau(0,H)\sec\theta} + (1-\epsilon_s)(T_{DN} + T_C e^{-\tau(0,\infty)\sec\theta}) e^{-\tau(0,H)\sec\theta} \quad (1)$$

where $T_s$ is the thermodynamic temperature of the surface in Kelvin, $\epsilon_s$ is the emissivity of the surface, $(1-\epsilon_s)$ is the reflectivity of the surface, $H$ is the satellite height in km, $T_C$ is the cosmic radiation, and $T_{DN}$ is given by

$$T_{DN} = \sec\theta \int_0^\infty T(z)\alpha(f,z) e^{-\tau(0,z)\sec\theta}\, dz \quad (2)$$

The upwelling brightness temperature in the zenith direction is given by

$$T_{UP} = \int_0^H T(z)\alpha(f,z) e^{-\tau(z,H)}\, dz \quad (3)$$

where $\theta$ is the incidence angle of the radiation, which is measured with respect to the normal ofthe surface, $\alpha(f,z)$ is the atmospheric attenuation in Nepers/km at frequency $f$ and height $z$, $\tau(0,z)$ is the opacity of the atmosphere between altitude 0 and $z$, and $T(z)$ is the air temperature at height $z$. The opacity measures the total amount of extinction suffered through the path and is given by

$$\tau(0,z) = \int_0^z \alpha(f,z')\, dz' \quad (4)$$

where the absorption coefficient $\alpha(f,z)$ accounts for both water vapor and oxygen absorption (assuming a nonscattering, clear atmosphere).

In (1), $T_C$ is the cosmic background radiation incident on the atmosphere from the top. The cosmic radiation at microwave frequencies varies with frequency as

$$T_C = 2.69 + 0.003\,625 f \quad (5)$$

which has an average of 2.78 K for the 20–32 GHz range. The frequency dependence accounts for the variable inaccuracy of the Rayleigh-Jeans approximation [11].

Equation (1) contains all the quantities needed to compute the response of a satellite-based microwave radiometer to changes in atmospheric and surface variables. In order to test models for surface emissivity against observations of $T_B$, we will need to estimate each of the other components of the model using ancillary data sources.

## II. Components of the Brightness Temperature Model

### A. Specular Sea Surface Emissivity Model

The specular emissivity of the ocean is a function of the frequency of operation and the dielectric properties of the sea water. If the ocean surface fills a flat half-space, the emissivity at normal incidence is given by

$$\epsilon_{spec} = 1 - \left| \frac{1-\sqrt{\varepsilon}}{1+\sqrt{\varepsilon}} \right|^2 \quad (6)$$

where the second term on the right is the Fresnel reflection coefficient at nadir and $\varepsilon$ is the dielectric coefficient of the sea water. The dielectric coefficient of sea water at microwave frequencies below 40 GHz can be represented by a simple Debye relaxation expression, given by

$$\varepsilon(f,T,S) = \varepsilon_\infty + \frac{\varepsilon_s - \varepsilon_\infty}{1 - j2\pi\tau f} + j\frac{\sigma}{2\pi f \varepsilon_o} = \varepsilon_R - j\varepsilon_I \quad (7)$$

where $\varepsilon_s$ and $\varepsilon_\infty$ are, respectively, the static and high frequency dielectric coefficients of the sea water, $\varepsilon_o$ is the permittivity of free space ($= 8.85\times10^{-12}$ F/m), $\tau$ is relaxation time in seconds, $\sigma$ is the ionic conductivity of the dissolved salts in mho/m, and $f$ is the frequency in Hertz. The real and imaginary parts of the permittivity are $\varepsilon_R$ and $\varepsilon_I$,, respectively. The parameters $\varepsilon_s$, $\varepsilon_\infty$, $\tau$, and $\sigma$ are all functions of the temperature $T$ and salinity $S$ of the sea water and are given by [14] and (more recently) by [7].

*1) Klein-Swift Ocean Dielectric Model:* The KS77 model uses a simple Debye expression for the sea water dielectric over a limited frequency range ($f < 10$ GHz) and polynomial fits for the static dielectric coefficient, the ionic conductivity, and the relaxation time as a function of temperature and salinity. The sea water dielectric coefficient model in KS77 was derived from dielectric measurements of sea water and aqueous NaCl solutions conducted at 1.43 and 2.65 GHz for salinities[1] in the range $4^0/_{00} < S < 35^0/_{00}$. Their derivation is based on the assumption that $\varepsilon_\infty$ has a constant value of 4.9 with uncertainty of $\pm$20%. Typical values of this parameter vary from 4.6 to 8.5 for salinity values between 23 and $39^0/_{00}$ and temperatures of 0–30 °C.

This model is still widely used for sea water dielectric coefficients, although the authors recommend care when using their model at frequencies above 10 GHz. They state that "as the frequency increases to X-band [8–12 GHz], ... the error in $\varepsilon'$ (the real part of $\varepsilon(f,T,S)$, here referred to as $\varepsilon_R$) is maximized" [14].

*2) Ellison Ocean Dielectric Model:* The E96 model was developed using water samples from the Mediterranean, Polar, Atlantic, and Mid-Atlantic Oceans. [7] improved the frequency range over that of KS77 and added a polynomial fit for the high frequency dielectric coefficient. They performed laboratory measurements of the dielectric coefficient for a wider range of frequencies (2–40 GHz), and at salinities ($20–40^0/_{00}$) and temperatures ($-2$ $-30$ °C), found in the worlds' oceans. Their claimed accuracy is 3% or better for frequencies of up to 40 GHz.

### B. Wind-Roughened Ocean Excess Emissivity Model

When the wind blows across the surface of the oceans, it generates roughness. This roughness increases the emissivity of the ocean. There are three mechanisms by which the wind-induced roughness increases the emission from the sea. The first one is the gravity waves. These are ocean waves with wavelengths that are long compared to the radiation wavelength and are modeled with the theory of geometric optics [23], [10], [31]. The second mechanism is capillary waves. These have wavelengths that are

[1]Salinity is expressed in parts per thousand ($^0/_{00}$) on a weight basis (i.e., total mass of solid salts in grams dissolved in one kilogram of solution).

small compared to the radiation wavelength and are modeled by small perturbation theory [29]. The third is the sea foam coverage over the ocean surface.

In the geometric optics approach, the ocean surface can be described by a series of reflecting flat facets with various inclinations characterized by a slope distribution. The individual contribution of each facet to the upwelling brightness temperature is calculated from the Fresnel reflection relations [3]. This approach was employed by [24] for 20 and 35 GHz frequencies, and by [10] for frequencies between 1 and 20 GHz. The latter study reveals that brightness temperatures are underestimated close to nadir. Furthermore, only fair agreement was obtained between model and measurements at 20 GHz, with increased degradation at lower frequencies.

To improve the agreement between theoretical predictions and low-frequency observations, a composite-surface model was developed [22], [34], [29]. This two-scale model combines geometric optics and small-scale perturbation theory by superimposing small capillary waves onto the larger gravity waves. The two-scale scattering model includes multiple reflections and shadowing effects. The model shows greater wind dependence at incidence angles away from nadir. The total nadir emissivity of the ocean can be expressed as [32]

$$\epsilon_s = \epsilon_{spec} + 0.0005^* W \quad \text{for } W < 7\text{m/s} \tag{8a}$$

$$= (\epsilon_{spec} + 0.0035)(1 - f_s) + f_s \quad \text{for } W > 7 \text{ m/s} \tag{8b}$$

where $W$ is the neutral stability wind speed at 19.5 m above the sea surface. The first term, $\epsilon_{spec}$, refers to the specular emission of the sea surface, and the second term refers to the effect of the wind-induced roughness on the ocean emissivity. For winds higher than 7 m/s, an additional term is added ($f_S$) to account for the effective fractional coverage of black body foam.

Foam cover increases the emissivity of the surface at a rate of about 1 K/m/s for wind speeds above 7 m/s at 19.35 GHz in the nadir direction [18], [25]. Since this work concentrates on calm to low wind speed conditions, the foam effect will not be considered here.

*1) Air-Sea Stability:* The wind varies with height near the surface of the ocean. This variation is affected by the temperature difference between the sea and the air on top. When the sea is warmer than the air, unstable conditions prevail and higher waves are generated for a given wind speed. When the air temperature is greater than the sea temperature, the condition is referred to as stable and the significant wave height is lower than that for neutral or unstable conditions. The wind speed measured by the altimeter is corrected to take into account the atmospheric stability conditions of the ocean. For this purpose, the sea surface temperature $\theta_s$ (see next section on NODC), the air temperature $\theta_a$, and the thermometer height $z_a$ (see next section about RaOb balloons) are used to compute the friction velocity $U^*$ and roughness parameter $z_o$ of the ocean [2]. The values found for $U^*$ and $z_o$ define the surface boundary layer wind distribution and are used to calculate the wind speed under neutral conditions at 19.5 m above the surface. This is the wind speed used in this analysis. It is referred to as the 19.5-m neutral stability wind.

### C. Atmospheric Absorption Models

*1) Liebe Model:* The atmospheric absorption model described by [15] (henceforth referred to as L93) is dominated in the microwave region by two Van Vleck-Weisskopf broadened water vapor lines at 22 and 183 GHz, together with an oxygen absorption complex of lines taken from [19], as well as a water vapor continuum term. Numerous parameters of the L93 model have been empirically fit to various observational data sets.

*2) Cruz Pol Model:* The atmospheric absorption model described in [4] (henceforth referred to as modL) is a modification to L93 that is based on a refined set of observations of atmospheric downwelling brightness temperature by a radiometer/spectrometer operating in the near vicinity of the 22 GHz water vapor line. A 1.3% increase in the line strength, together with a 6.6% increase in the line width of the 22 GHz absorption line, are determined to be statistically significant corrections to the L93 model within the range of 18–37 GHz.

## III. Data Sets

The data used here include measurements taken from December 1992 to May 1997 from three different sources. These sources are 1) the TOPEX/Poseidon satellite mission (both altimeter and radiometer); 2) 15 RaOb stations around the globe; and 3) the National Oceanographic Data Center (NODC). TOPEX altimeter data provides a measurement of the surface wind speed. RaOb profiles provide atmospheric emission and transmissivity and near-surface air temperature. NODC data provides sea surface temperature and salinity. These data sets are combined to model the $T_B$ observed by the TOPEX Microwave Radiometer (TMR), and the model is then compared with actual TMR measurements.

Screening of the data is intended to isolate only those cases most amenable to accurate modeling of the $T_B$. To this end, only low wind, cloud free, and low humidity cases are considered, and only data with near coincident TOPEX overpasses of radiosonde launches. Each data set is described in greater detail below.

### A. TOPEX/Poseidon: Altimeter Data

The dual-frequency altimeter provides ocean surface radar backscatter coefficient per unit area $\sigma_o$, from which sea surface wind speed can be estimated. A return pulse that has spread out in time is an indication of a rough ocean due to high winds. If the pulse comes back with high amplitude, it means there is a calm sea. In this way, the T/P altimeter pinpoints low wind conditions, at which time, the TMR measured brightness is due mainly to the specular sea emissions.

The altimeter $\sigma_o$ at Ku band in the range of 10 to 20 dB was selected for the present analysis, since these values correspond to low wind conditions. The modified Chelton-Wentz (MCW) [33] table as calibrated for TOPEX [1] was used to convert the $\sigma_o$ values to wind speed at a height of 19.5 m above the ocean surface. TOPEX $\sigma_o$ values are reduced by 0.63 dB before using MCW to fine tune the absolute calibration [Callahan, personal communication, 1998].

Use of the MCW algorithm results in an RMS error of $\pm 1.4$ m/s and a bias of $-0.4$ m/s for winds less than 23 m/s [1]. Only

data with winds below 7 m/s, at which speeds surface foaming is negligible, are utilized in order to isolate low wind conditions and relax the dependence of our correction to the specular model on the accuracy of the wind model.

### B. TOPEX Microwave Radiometer (TMR)

The TMR is a nadir-viewing radiometer that measures the water vapor content in the atmosphere by measuring the brightness temperature from the ocean surface at 18, 21, and 37 GHz [21]. Temperatures are measured every second. Internal hot and cold calibrations are performed alternately every 14 s. Corrections of $-0.28$, $-0.07$, and $-0.04$ K/year were added to each of the three frequency channels, respectively, to correct for drifts in the receiver calibration [13]. TMR measurements of the ocean surface brightness temperature have an instrument RMS precision of 0.3 K and an absolute accuracy of 0.8 K.

*1) TMR Data Selection and Screening:* All three TMR brightnesses are used to filter out data points that have integrated liquid water content greater than 100 $\mu$m to ensure clear sky conditions. The liquid cloud content is computed from the following algorithm [13]

$$\begin{aligned} Liq &= L_0 + L_{corr} \\ L_0 &= -2280.36 - 12.241TB_{18} - 5.128TB_{21} \\ &\quad + 28.964TB_{37} \quad \text{and} \\ L_{corr} &= \begin{cases} 0, & \text{if } L_0 < 600 \\ 0.43(L_0 - 600 + .0003(L_0 - 600)^2, & \text{if } L_0 \geq 600. \end{cases} \end{aligned} \tag{9}$$

Only TMR brightness temperatures at 18 and 37 GHz are used to test the two emissivity models, since 21 GHz is much more sensitive to humidity and introduces significantly larger errors in the estimation of ocean emissivity.

### C. Radiosonde Data

Data from thirty (30) RaOb launch stations around the globe were compiled. At each station, a RaOb balloon was launched at most four times a day. The atmospheric profiles include air temperature, pressure, and dew point temperature from which the relative humidity is computed using the Goff-Gratch formulation [8].

Uncertainties in the RaOb reading are given in [6] as $\pm 0.7$ mbar for barometric pressure, $\pm 0.84$ K for air temperature, and $\pm 5\%$ for relative humidity. To ensure that only clear (no clouds) atmosphere data were employed in the analysis, profiles with relative humidity values greater than 94% were filtered out, since this indicates the possible presence of clouds.

The profiles were used to compute the upwelling and downwelling temperatures, and the transmissivity and the path delay of the atmosphere. Only profiles with path delay of less than 15 cm were used in order to reduce the sensitivity of the new ocean model to the accuracy of the atmosphere model. A histogram of the path delay values in the final data set is shown in Fig. 1(a).

The values for the remaining RaOb-derived variables range from 5.1 K to 13.4 K for $T_{up}$, from 7.7 K to 16.0 K for $T_{dn}$, and from 0.95 to 0.98 for $e^{-\tau}$ at 18 GHz. They range from 13.9 K to 26.2 K for $T_{up}$, from 16.6 K to 28.8 K for $T_{dn}$, and from 0.91 to 0.95 for $e^{-\tau}$ at 37 GHz.

The time and space separation between RaOb stations and TMR measurements was limited to 6 h and 300 km, respectively. After the data were filtered for clouds, low winds, path delay, and time and space separation, only data from 15 radiosonde stations were actually utilized in the analysis, more specifically from stations with legend numbers 1, 6 to 14, 20, 24, and 28 to 30 (see Table I), which yields a total of 263 RaOb profiles.

### D. National Oceanographic Data Center (NODC) Ocean Temperature and Salinity Profiles

The NODC provides depth profiles of ocean temperature and salinity measurements taken between 1900 and 1990 [17]. Values of temperature and salinity at the surface (zero-depth) were used. For each of the 15 radiosonde stations used, a $10 \times 10$ degree latitude/longitude cell was identified. For each month of the year and each $10 \times 10$ ° cell, the average value of all surface salinities and temperatures reported over the 90-year data set within that cell were used as our best estimate of the true conditions. The standard deviations over the 90 years was used as a measure of the RMS error associated with each average value. All the averaged values of sea surface temperature and salinity and their corresponding standard deviations for each month and radiosonde station are tabulated in Table III.

The range of values for sea surface temperature and salinity used in this analysis is presented in the two histograms shown in Fig. 1(b), (c). Typical values for salinity range from 34 to $36^0/_{00}$ and with a few showing up at around $30^0/_{00}$. Sea surface temperature values ranges from 5 to 30 °C.

### E. Screening of the Data Sets

Only data close to the TOPEX ground track in time (< 6 h) and proximity (less than 300 km) were employed in the analysis. The temporal separation of 6 h was chosen because the radiosonde balloons are usually launched every 12 h. The separation between two TOPEX passes near the equator ground track is approximately 150 km. Therefore, choosing 300 km for spatial separation allows for more than one pass to be near to a radiosonde station in case the other satellite pass is longer than 6 h in time. The closest data point from TMR for every radiosonde station measurement was used for comparison.

After all the data were filtered for no clouds, low wind speed, low humidity, and space and time colocation, we were left with a total of 263 RaOb profiles available with corresponding TOPEX altimeter and radiometer data. The total number of modeled versus measured $T_B$ data points is then 526, since we are using the two frequency channels 18 and 37 GHz.

## IV. Analysis and Results

### A. Evaluation Metrics for Previous Models

The performance of the different dielectric models of the ocean were evaluated using a number of metrics. The RMS difference between the modeled and measured $T_B s$ was computed at each frequency. The average difference, or bias, between the

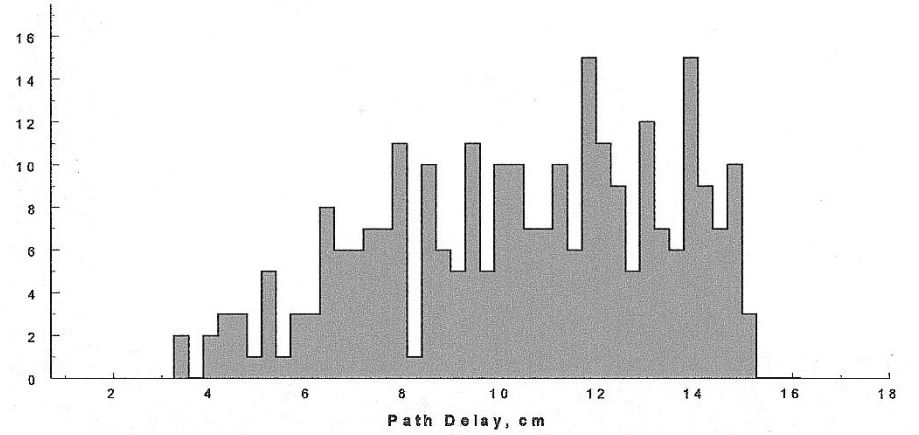


(a)

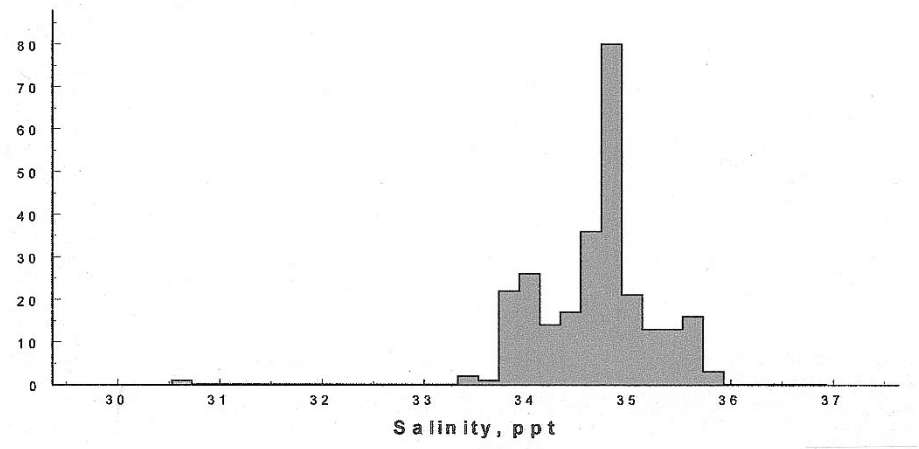


(b)

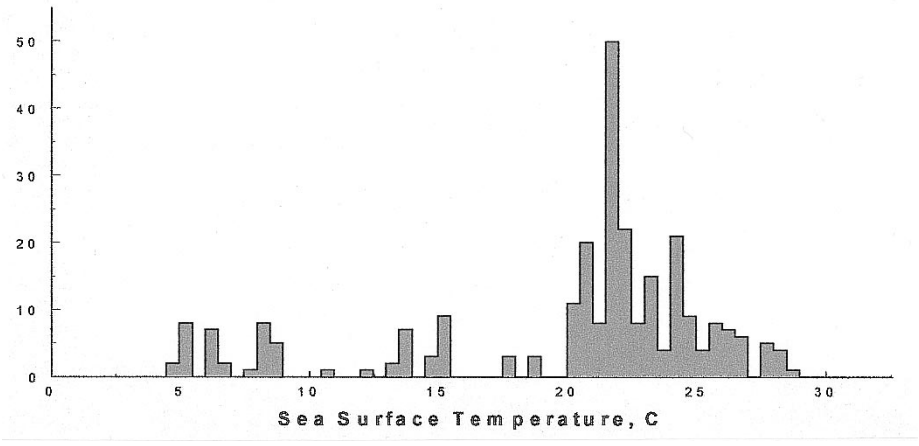


(c)

Fig. 1. Histograms of the range of: (a) path delays, (b) salinity, and (c) sea surface temperatures for the data used in this work.

two $T_Bs$ was also computed at each frequency. Another metric, the frequency dependence of the bias, is defined as

$$\text{frequency dependence} = ave\Delta T_{18} - ave\Delta T_{37} \tag{10}$$

where $ave\Delta T_f$ is the error in brightness $(TB_{TMR} - TB_{model})$ averaged over all 263 data points at the frequency $f$. This parameter is an indication of the confidence with which the model can be extrapolated to higher frequencies.

TABLE I
COORDINATES OF THE RADIOSONDE STATIONS

| Legend No. | Station Code Name | Latitude (N is +) | Longitude (E is +) |
|---|---|---|---|
| 1 | 6011 | 62.01 | -6.46 |
| 2 | 8301 | 39.33 | 2.37 |
| 3 | 8522 | 32.38 | -16.54 |
| 4 | 16429 | 37.55 | 12.3 |
| 5 | 32618 | 55.12 | 165.59 |
| 6 | 43311 | 11.07 | 72.44 |
| 7 | 43333 | 11.4 | 92.43 |
| 8 | 43369 | 8.18 | 73.09 |
| 9 | 47678 | 33.06 | 139.47 |
| 10 | 47909 | 28.23 | 129.3 |
| 11 | 47936 | 26.12 | 127.41 |
| 12 | 47945 | 25.5 | 131.14 |
| 13 | 47971 | 27.05 | 142.11 |
| 14 | 47991 | 24.18 | 153.58 |
| 15 | 61901 | -15.56 | -5.4 |
| 16 | 61902 | -7.58 | -14.24 |
| 17 | 61967 | -7.18 | 72.24 |
| 18 | 61996 | -37.48 | 77.32 |
| 19 | 68906 | -40.21 | -9.53 |
| 20 | 68994 | -46.53 | 37.52 |
| 21 | 71600 | 43.56 | -60.01 |
| 22 | 78016 | 32.22 | -64.41 |
| 23 | 91217 | 13.33 | 144.5 |
| 24 | 91245 | 19.17 | 166.39 |
| 25 | 91348 | 6.58 | 158.13 |
| 26 | 91413 | 9.29 | 138.05 |
| 27 | 91643 | -8.31 | 179.13 |
| 28 | 94299 | -16.18 | 149.59 |
| 29 | 94996 | -29.02 | 167.56 |
| 30 | 96996 | -12.11 | 96.49 |

The sensitivity of errors in the ocean model to temperature and salinity is estimated using the $R^2$ value of a linear regression fit of the difference between modeled and measured $T_B$ versus the variables temperature $T_{sea}$ or salinity $S$. In this context, the $R^2$ is a measure of how much of the error is dependent on the variable. Therefore, the smaller this value is the better, since errors in the model should not be sensitive to either of these two variables. As an example, Fig. 2 shows a plot and linear fit of the ocean model error versus $T_{sea}$ for E96. The $R^2$ value is found to be small. This is an indication that errors are not highly dependent on the sea surface temperature or salinity of the ocean.

The obtained values for the RMS difference, bias, and dependence on salinity, temperature, and frequency are shown on Table II for both ocean emissivity models, E96 and KS77. Both models are shown first with the L93 atmospheric absorption model. The models are also shown using the modL atmospheric model developed in [4].

As seen in Table II, all combinations of models have a negligible dependence on salinity and sea surface temperature. On the other hand, the frequency dependence of KS77-L93 is very large: −2.88 K. This is not surprising, since this model was meant to be valid only for frequencies less than 10 GHz (although it is commonly used for higher frequencies). The

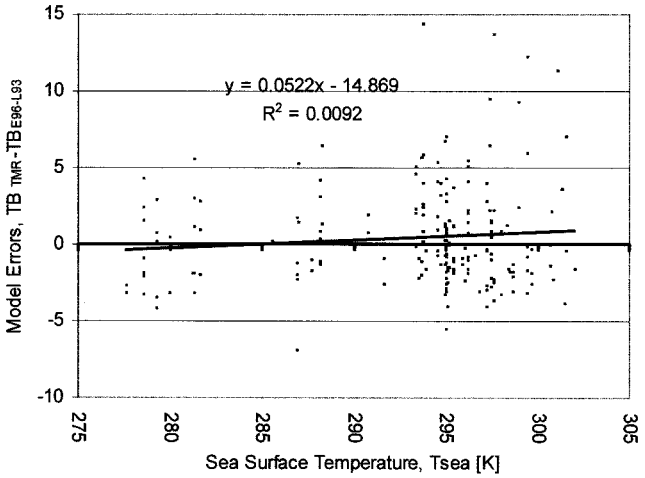


Fig. 2. Plot of the model error ($TB_{TMR} - TB_{model}$) versus the sea surface temperature for E96. The $R^2$ value of the linear fit is shown to be small, denoting a small dependence of the error in this model on the sea surface temperature.

E96-L93 model improves the frequency dependence (down to −2.30 K) as well as the RMS and bias.

The RMS and bias shown in the first two entries of Table II agree with results previously presented by [7]. They showed an improvement in the RMS with their E96 ocean model over KS77, as well as a lower bias when using L93. However, when the new atmospheric model, modL, is applied, the RMS and bias for the KS77 model are superior. On the other hand, E96 maintains its superior frequency dependence. This is to be expected, since the E96 ocean dielectric model was developed from measurements at frequencies of up to 40 GHz. For both surface models, the frequency dependence with the new atmospheric model shows a small decrease from the one exhibited when using L93 (2.30 K and 1.74 K), but this dependence is still quite large when one considers the potential error from extrapolating either model to much higher frequencies (e.g., the 85–90 GHz atmospheric window).

### *B. Modified Dielectric Model Parameter Estimation*

In order to reduce the sensitivity of the error to frequency as well as reduce the RMS difference and bias, both the KS77 and L96 ocean models are parameterized and adjusted to "best fit" the TMR data at 18 and 37 GHz using the Newton-Raphson method. The performance of each modified model is then evaluated using the same metrics described above.

Both E96 and KS77 are based on a simple Debye equation with different polynomial functions for $\varepsilon_s$, $\varepsilon_\infty$, $\tau$, and $\sigma$. They define the real and imaginary parts of the permittivity as

$$\varepsilon_R = \varepsilon_\infty + \frac{\varepsilon_s - \varepsilon_\infty}{1 + (2\pi f\tau)^2} \tag{11}$$

and

$$\varepsilon_I = \frac{2\pi f\tau(\varepsilon_s - \varepsilon_\infty)}{1 + (2\pi f\tau)^2} + \frac{\sigma}{2\pi\varepsilon_o f}. \tag{12}$$

We introduce two new parameters, $c_R$ and $c_I$, which are scaling factors to the real and imaginary parts, or

$$\varepsilon(f, T, S) = c_R\varepsilon_R - jc_I\varepsilon_I. \tag{13}$$

TABLE II
COMPARISON AMONG OCEAN EMISSIVITY MODELS

| Model | | Overall RMS | Bias [K] | | Salinity Dependence | | $T_{sea}$ Dependence | | Frequency dependence |
|---|---|---|---|---|---|---|---|---|---|
| Ocean | Atmosphere | [K] | 18GHz | 37GHz | 18 GHz | 37GHz | 18 GHz | 37GHz | [K] |
| KS77 | L93 | **3.55** | -0.16 | 2.72 | 0.0901 | 0.0093 | 0.0037 | 0.0264 | -2.88 |
| E96 | L93 | **3.27** | -1.63 | 0.66 | 0.0993 | 0.0218 | 0.0001 | 0.0021 | -2.30 |
| KS77 | ModL | **3.28** | -0.67 | 1.63 | 0.0822 | 0.0112 | 0.0017 | 0.0175 | -2.30 |
| E96 | ModL | **3.45** | -2.14 | -0.41 | 0.1012 | 0.0243 | 0.0008 | 0.0003 | -1.74 |
| ModKS ($c_R$=1.12 , $c_I$=.961) | ModL | **3.03** | -0.29 | 0.27 | 0.0368 | 0.0056 | 0.0564 | 0.0410 | -0.56 |
| ModE ($c_R$=1.15 , $c_I$=1.001) | ModL | **2.98** | -0.16 | 0.14 | 0.0555 | 0.0154 | 0.0219 | 0.0078 | -0.30 |

Retrieval of the adjustable parameters $c_R$ and $c_I$ begins by forming the Jacobian matrix

$$J = \begin{bmatrix} \dfrac{\partial T_{B1}}{\partial c_R} & \dfrac{\partial T_{B1}}{\partial c_I} \\ \dfrac{\partial T_{B2}}{\partial c_R} & \dfrac{\partial T_{B2}}{\partial c_I} \\ \vdots & \vdots \\ \dfrac{\partial T_{Bn}}{\partial c_R} & \dfrac{\partial T_{Bn}}{\partial c_I} \end{bmatrix} \tag{14}$$

where $n = 526$ is the total number of comparison data points, and the derivatives are evaluated numerically. The initial estimate of the parameters is $c_R = c_I = 1$. An update to the estimate is made using

$$\vec{c}_{new} = \begin{bmatrix} c_R \\ c_I \end{bmatrix} = \vec{c}_{initial} + \Delta\vec{c} \tag{15}$$

where $\Delta\vec{c}$ is the correction to the parameters and is computed by minimum square error (MSE) inversion as

$$\Delta\vec{c} = (J^t J)^{-1} J^t \Delta\vec{T}_B. \tag{16}$$

The process is iterated until successive estimates of the parameters are nearly identical. The number of iterations indicates how easily the retrieval converges. It is a measure of the sensitivity of the available data to the parameters being retrieved. The maximum allowed number of iterations was chosen as ten, since when the iteration number is ten or larger, convergence is rarely attained and the retrieved values are not reliable. Both of the modified models converge rapidly (in three iterations).

The final estimates of the parameters are $c_R = 1.12$ and $c_I = 0.961$ for KS77, and $c_R = 1.15$ and $c_I = 1.001$ for E96. These modified versions of KS77 and E96 will be referred to as ModKS and ModE in the remainder of this work. The resulting RMS difference, bias, salinity, temperature and frequency dependence for the nominal and modified models are presented in Table II.

The bias in the modified models is significantly decreased, to about $-0.16$ K for ModE and to about $-0.3$ K for ModKS at both frequencies. The frequency dependence is also lowered, to $-0.56$ K and $-0.30$ K for ModKS and ModE, respectively. The overall RMS difference for both modified ocean models decreases to 3.03 K and 2.98 K, respectively. The RMS error in brightness temperature is decreased for both modified models, and the average difference is at most $-0.29$ K. The temperature and salinity dependence are also kept small for the new ocean emissivity models.

A comparison between the two modified models suggests that ModE has a superior overall performance to that of ModKS. It has the lowest bias. Its frequency dependence is half of that exhibited by ModKS, which will allow for more reliable extrapolation to higher frequencies. For example, a frequency dependence of $-.30$ K, which was computed for a frequency difference of $37 - 18 = 19$ GHz, implies that at 85 GHz, the bias error will be only $-0.30(85 - 18)/(37 - 18) = 1.06$ K. Using the ModKS model yields double this amount. In addition, ModE has a lower dependence on sea surface temperature and a lower RMS difference. The salinity dependence is still acceptably small, also. For these reasons, ModE is the model that we would recommend for future remote sensing applications involving microwave emissions from the ocean.

## V. ERROR ANALYSIS

A numerical sensitivity analysis was conducted to determine the level of uncertainty in the estimated parameters due to measurement noise by the radiometer, errors in the altimeter-derived wind, RaObs, NODC data, and decorrelation between the TMR and RaOb data. Independent realizations of the entire estimation process were simulated, in which random perturbations were made to the actual measurements in a manner consistent with their estimated errors. The RMS variation in the resulting realizations of the estimated parameters is taken as the accuracy of the parameters given the errors in the input data sets.

The spatial and time decorrelation between TMR and RaOb measurements introduces an additional error. This error was estimated by Ruf *et al.* in [20], who found that, for an average separation distance of 150 km, there is a 2.3 cm spatial decorrelation error in the path delay measurement. For a mean time separation of 2.9 h, the time decorrelation error is 1.4 cm. In our data set, the average distance separation is 142 km, and the mean time separation is 3.1 h. Therefore, these values for decorrelation errors can be used as a conservative estimate. These errors have to be translated into equivalent errors in $T_B$. For this reason, the correspondence between path delay and brightness was found at all three frequencies from the slope of their respective scatter plots versus path delay. The slopes are found to

TABLE III
TABLE OF MEAN STANDARD DEVIATION AND COUNTS OF SEA SURFACE TEMPERATURE AND SALINITY PER MONTH PER RAOB STATION FOR THE PERIOD OF 1900 TO 1990

| | Jan | Feb | Mar | Apr | May | Jun | Jul | Aug | Sept | Oct | Nov | Dec |
|---|---|---|---|---|---|---|---|---|---|---|---|---|
| **Station 6** | | | | | | | | | | | | |
| Mean Tsea | 300.8 | 300.75 | 302.1 | 303.46 | 303.66 | 302.24 | 301.56 | 301.39 | 301.01 | 301.34 | 301.83 | 301.56 |
| Tsea-Std. dev. | 0.6 | 1.04 | 0.87 | 1.01 | 0.82 | 0.67 | 0.72 | 0.43 | 0.98 | 0.99 | 0.62 | 0.54 |
| Mean Salinity | 34.05 | 33.96 | 34.49 | 34.54 | 35.14 | 35.36 | 35.34 | 33.98 | 34.98 | 35.22 | 34.65 | 34.56 |
| Salinity-Std. dev. | 1.13 | 0.69 | 0.66 | 0.51 | 0.49 | 0.92 | 2.01 | 3.46 | 1.41 | 0.98 | 1.24 | 1.26 |
| Counts | 56 | 18 | 87 | 108 | 49 | 36 | 72 | 29 | 31 | 43 | 111 | 93 |
| **Station 7** | | | | | | | | | | | | |
| Mean Tsea | 299.42 | 300.26 | 301.41 | 302.46 | 303.17 | 301.89 | 302.07 | 301.87 | 301.11 | 301.31 | 301.05 | 299.98 |
| Tsea-Std. dev. | 0.45 | 1.08 | 0.75 | 1.17 | 0.12 | 0.25 | 0.37 | 0.72 | 0.32 | 0.47 | 0.22 | 0.86 |
| Mean Salinity | 30.53 | 31.89 | 32.55 | 31.96 | 32.39 | 33.09 | 33.1 | 32.74 | 32.7 | 32.59 | 31.55 | 28.15 |
| Salinity-Std. dev. | 1.6 | 1.28 | 0.49 | 0.77 | 0.28 | 0.32 | 0.33 | 0.57 | 0.91 | 0.78 | 0.06 | 2.88 |
| Counts | 21 | 18 | 135 | 9 | 4 | 2 | 68 | 4 | 41 | 57 | 2 | 31 |
| **Station 8** | | | | | | | | | | | | |
| Mean Tsea | 301.48 | 301.55 | 302.41 | 303.05 | 302.66 | 301.9 | 301.22 | 300.91 | 300.12 | 300.76 | 301.9 | 301.62 |
| Tsea-Std. dev. | 0.36 | 0.58 | 0.56 | 0.56 | 1.12 | 0.72 | 0.95 | 1.32 | 1.32 | 0.98 | 0.73 | 0.43 |
| Mean Salinity | 33.56 | 33.94 | 34.15 | 34.52 | 34.65 | 34.87 | 34.68 | 34.46 | 34.22 | 35.09 | 34.69 | 33.65 |
| Salinity-Std. dev. | 1.1 | 0.59 | 0.54 | 0.41 | 0.94 | 0.94 | 1.81 | 2.54 | 2.75 | 0.88 | 1.47 | 1.16 |
| Counts | 38 | 100 | 31 | 107 | 39 | 46 | 55 | 62 | 92 | 98 | 83 | 53 |
| **Station 9** | | | | | | | | | | | | |
| Mean Tsea | 287.64 | 286.99 | 286.91 | 288.17 | 291.64 | 293.89 | 297.53 | 299.98 | 298.69 | 295.89 | 293.98 | 290.74 |
| Tsea-Std. dev. | 3.75 | 4.28 | 4.29 | 3.64 | 3.56 | 2.88 | 2.59 | 1.7 | 1.91 | 2.12 | 2.36 | 2.83 |
| Mean Salinity | 33.8 | 34.08 | 33.9 | 33.87 | 34.05 | 33.75 | 33.27 | 33.09 | 32.79 | 33.34 | 33.75 | 33.77 |
| Salinity-Std. dev. | 1.51 | 1.31 | 1.68 | 1.5 | 1.38 | 1.68 | 1.69 | 1.59 | 1.81 | 1.38 | 1.25 | 1.26 |
| Counts | 1986 | 3670 | 3393 | 2460 | 4796 | 3097 | 4449 | 5826 | 2882 | 4608 | 4222 | 2800 |
| **Station 10** | | | | | | | | | | | | |
| Mean Tsea | 293.77 | 293.34 | 294.52 | 295.15 | 297.43 | 298.73 | 301.55 | 302.03 | 301.07 | 298.94 | 297.4 | 296.16 |
| Tsea-Std. dev. | 2.85 | 2.95 | 2.79 | 4.06 | 2.58 | 1.88 | 1.09 | 0.81 | 1.04 | 1.5 | 1.4 | 2.49 |
| Mean Salinity | 34.69 | 34.66 | 34.76 | 34.44 | 34.43 | 33.97 | 33.95 | 34.05 | 34.14 | 34.23 | 34.4 | 34.55 |
| Salinity-Std. dev. | 0.28 | 0.27 | 0.24 | 0.61 | 0.59 | 0.99 | 0.72 | 0.63 | 0.81 | 0.38 | 0.4 | 0.3 |
| Counts | 348 | 599 | 340 | 428 | 686 | 560 | 513 | 795 | 401 | 664 | 453 | 137 |
| **Station 11** | | | | | | | | | | | | |
| Mean Tsea | 293.77 | 293.34 | 294.52 | 295.15 | 297.43 | 298.73 | 301.55 | 302.03 | 301.07 | 298.94 | 297.4 | 296.16 |
| Tsea-Std. dev. | 2.85 | 2.95 | 2.79 | 4.06 | 2.58 | 1.88 | 1.09 | 0.81 | 1.04 | 1.5 | 1.4 | 2.49 |
| Mean Salinity | 34.69 | 34.66 | 34.76 | 34.44 | 34.43 | 33.97 | 33.95 | 34.05 | 34.14 | 34.23 | 34.4 | 34.55 |
| Salinity-Std. dev. | 0.28 | 0.27 | 0.24 | 0.61 | 0.59 | 0.99 | 0.72 | 0.63 | 0.81 | 0.38 | 0.4 | 0.3 |
| Counts | 348 | 599 | 340 | 428 | 686 | 560 | 513 | 795 | 401 | 664 | 453 | 137 |
| **Station 12** | | | | | | | | | | | | |
| Mean Tsea | 294.71 | 293.52 | 293.65 | 294.89 | 296.58 | 298.94 | 301.15 | 301.73 | 301.53 | 299.77 | 297.93 | 295.9 |
| Tsea-Std. dev. | 1.63 | 1.62 | 1.83 | 1.81 | 1.71 | 1.97 | 1.41 | 0.86 | 1.01 | 1.26 | 1.41 | 1.54 |
| Mean Salinity | 34.81 | 34.86 | 34.83 | 34.82 | 34.77 | 34.61 | 34.5 | 34.47 | 34.54 | 34.63 | 34.63 | 34.67 |
| Salinity-Std. dev. | 0.14 | 0.16 | 0.16 | 0.14 | 0.17 | 0.23 | 0.28 | 0.25 | 0.19 | 0.2 | 0.2 | 0.16 |
| Counts | 469 | 306 | 269 | 256 | 365 | 427 | 379 | 443 | 310 | 382 | 344 | 160 |
| | **Jan** | **Feb** | **Mar** | **Apr** | **May** | **Jun** | **Jul** | **Aug** | **Sept** | **Oct** | **Nov** | **Dec** |
| **Station 13** | | | | | | | | | | | | |
| Mean Tsea | 294.98 | 295.4 | 294.99 | 295.28 | 297.47 | 299.87 | 301.9 | 301.39 | 301.55 | 300.68 | 299.23 | 297.63 |
| Tsea-Std. dev. | 2.31 | 2.75 | 2.42 | 2.73 | 2.31 | 1.72 | 1.05 | 0.84 | 0.59 | 1.09 | 1.87 | 1.63 |

be 0.985, 1.99, and 0.985 K/cm, respectively, at 18, 21, and 37 GHz. From this, it can be deduced that the decorrelation error is the same for both the 18 and 37 GHz frequencies, and it approximately doubles at 21 GHz. Consequently, the spatial and time decorrelation errors are estimated at 2.27 K and 1.38 K, respectively, for both the 18 and 37 GHz channels. The 21 GHz data was not utilized, since its enhanced sensitivity to water vapor introduces additional uncertainty in the retrieval of the ocean parameters.

Possible biases in the absolute calibration of the radiometer were modeled as an additive constant brightness temperature. Realizations of the TMR biases are selected from a zero mean, normally distributed, random process with standard deviation of 0.8 K. Additive random noise in the radiometer data was also

TABLE III *(Continued.)*
TABLE OF MEAN STANDARD DEVIATION AND COUNTS OF SEA SURFACE TEMPERATURE AND SALINITY PER MONTH PER RAOB STATION FOR THE PERIOD OF 1900 TO 1990

| | | | | | | | | | | | | |
|---|---|---|---|---|---|---|---|---|---|---|---|---|
| Mean Salinity | 34.88 | 34.89 | 35 | 34.94 | 34.88 | 34.85 | 35.05 | 34.69 | 34.9 | 34.8 | 34.8 | 34.78 |
| Salinity-Std. dev. | 0.13 | 0.26 | 0.26 | 0.18 | 0.17 | 0.18 | 0.36 | 0.27 | 0.26 | 0.22 | 0.13 | 0.18 |
| Counts | 49 | 89 | 143 | 93 | 58 | 66 | 36 | 191 | 83 | 73 | 60 | 22 |
| **Station 14** | | | | | | | | | | | | |
| Mean Tsea | 295.01 | 296.22 | 295.05 | 297.22 | 298.98 | 299.81 | 300.88 | 300.31 | 300.54 | 301.64 | 299.86 | 297.24 |
| Tsea-Std. dev. | 2.08 | 1.98 | 2.5 | 2.75 | 1.62 | 1.66 | 1.46 | 1.2 | 1.1 | 0.4 | 1.8 | 2.19 |
| Mean Salinity | 34.75 | 35.06 | 35.07 | 35.07 | 35.02 | 34.97 | 34.91 | 34.83 | 35 | 34.73 | 34.95 | 34.79 |
| Salinity-Std. dev. | 0.31 | 0.19 | 0.15 | 0.18 | 0.2 | 0.22 | 0.36 | 0.23 | 0.06 | 0.06 | 0.22 | 0.2 |
| Counts | 19 | 26 | 38 | 38 | 31 | 74 | 25 | 82 | 2 | 2 | 24 | 26 |
| **Station 20** | | | | | | | | | | | | |
| Mean Tsea | 278.52 | 281.22 | 281.27 | 281.62 | 281.73 | 279.96 | 280.52 | 277.6 | 285.54 | 286.57 | 288.24 | 279.22 |
| Tsea-Std. dev. | 1.48 | 4.17 | 3.01 | 4.57 | 11.83 | 2.62 | 4.5 | 2.38 | 0.79 | 0 | 0 | 3.43 |
| Mean Salinity | 34.01 | 34.01 | 34.09 | 34.17 | 34.1 | 33.99 | 34.23 | 33.87 | 34.94 | 35.17 | 35.44 | 34.2 |
| Salinity-Std. dev. | 0.09 | 0.5 | 0.39 | 0.67 | 1.32 | 0.38 | 0.7 | 0.07 | 0.11 | 0 | 0 | 0.44 |
| Counts | 2 | 31 | 4 | 11 | 3 | 5 | 2 | 2 | 2 | 1 | 1 | 3 |
| **Station 24** | | | | | | | | | | | | |
| Mean Tsea | 300.69 | 300.34 | 299.69 | 300.23 | 300.76 | 301.03 | 301.02 | 301.5 | 301.95 | 302.03 | 301.52 | 300.52 |
| Tsea-Std. dev. | 0.57 | 0.45 | 0.72 | 0.44 | 0.35 | 0.35 | 1.23 | 0.42 | 0.23 | 0.17 | 0.14 | 0.77 |
| Mean Salinity | 34.45 | 34.64 | 34.63 | 34.8 | 34.69 | 34.69 | 34.62 | 34.8 | 34.75 | 34.67 | 34.38 | 34.52 |
| Salinity-Std. dev. | 0.25 | 0.29 | 0.23 | 0.24 | 0.22 | 0.31 | 0.23 | 0.22 | 0.18 | 0.15 | 0.1 | 0.29 |
| Counts | 23 | 9 | 20 | 9 | 95 | 78 | 38 | 57 | 35 | 9 | 16 | 25 |
| **Station 28** | | | | | | | | | | | | |
| Mean Tsea | 301.37 | 301.14 | 301.52 | 300.89 | 299.92 | 299.12 | 298.64 | 298.32 | 298.64 | 299.68 | 301.44 | 301.32 |
| Tsea-Std. dev. | 0.57 | 0 | 0.48 | 0.79 | 0.65 | 0.75 | 1.27 | 1.01 | 1.19 | 0.72 | 1 | 1 |
| Mean Salinity | 35 | 36.11 | 34.03 | 34.57 | 34.61 | 34.93 | 35.5 | 35.26 | 35.31 | 35.42 | 35.28 | 35.49 |
| Salinity-Std. dev. | 0.72 | 0 | 0.93 | 0.9 | 0.3 | 0.17 | 0.47 | 0.21 | 0.29 | 0.27 | 0.35 | 0.53 |
| Counts | 7 | 1 | 14 | 18 | 54 | 16 | 11 | 9 | 27 | 21 | 46 | 22 |
| **Station 29** | | | | | | | | | | | | |
| Mean Tsea | 299.61 | 299.41 | 299.43 | 299.65 | 298.41 | 296.74 | 295.23 | 294.9 | 296.78 | 295.99 | 297.97 | 298.63 |
| Tsea-Std. dev. | 0.78 | 0.69 | 1.47 | 1.17 | 1.06 | 1.15 | 1.35 | 1.5 | 0.86 | 0.68 | 1.04 | 1.16 |
| Mean Salinity | 35.32 | 35.53 | 35.49 | 35.37 | 35.5 | 35.53 | 35.61 | 35.54 | 35.56 | 35.64 | 35.8 | 35.15 |
| Salinity-Std. dev. | 0.26 | 0.27 | 0.26 | 0.16 | 0.21 | 0.2 | 0.12 | 0.21 | 0.25 | 0.13 | 0.23 | 0.24 |
| Counts | 78 | 236 | 30 | 144 | 286 | 73 | 33 | 43 | 275 | 19 | 161 | 112 |
| **Station 30** | | | | | | | | | | | | |
| Mean Tsea | 300.51 | 300.83 | 301.44 | 300.83 | 300.35 | 299.11 | 298.58 | 298.12 | 298.5 | 298.77 | 299.81 | 299.67 |
| Tsea-Std. dev. | 0.89 | 0.25 | 0.67 | 0.93 | 0.48 | 1.46 | 1.99 | 1.89 | 0.52 | 0.95 | 0.46 | 0.87 |
| Mean Salinity | 34.52 | 33.85 | 34.37 | 34.21 | 34.18 | 34.59 | 34.43 | 34.39 | 34.42 | 34.53 | 34.1 | 34.64 |
| Salinity-Std. dev. | 0.39 | 0.19 | 0.34 | 0.26 | 0.07 | 0.29 | 0.38 | 0.34 | 0.2 | 0.23 | 0.36 | 0.22 |
| Counts | 7 | 2 | 4 | 10 | 7 | 11 | 6 | 8 | 7 | 14 | 5 | 8 |

modeled. This noise is independent for every radiometer measurement and RaOb profile and is normally distributed with zero mean and a standard deviation of 2.95 K (2.65 decorrelation in time and space plus 0.3K instrument RMS noise). RaOb uncertainties were simulated in the same way as the RaOb data set in [4]. In summary, errors in temperature, pressure, and humidity were all modeled as normally distributed with both a bias and random component as determined by the accuracy values specified previously in Section III-C.

Uncertainties in the NODC salinity and temperature readings are modeled as both a bias error and a random error. The possibility of a consistent bias in the NODC data set comes about because any particular radiosonde station is fixed in space somewhere within its $10 \times 10$ degree latitude/longitude cell (see Section III-D for details). There may be a persistent difference between the temperature or salinity at that location versus the average over the cell. This bias is estimated as the standard deviation of all NODC points within a cell at a given month. For sea temperature readings, this bias was found to be approximately 1.0 K. For salinity readings, the value was found to be $0.7^{0}/_{00}$.. The NODC random errors are both normally distributed with zero mean and standard deviations, as given in the Table III. They are varied for each individual reading and for every noise realization.

For the altimeter-derived winds, the uncertainties are again modeled as a bias plus a random, normally distributed error. The bias is the same for wind values at each noise realization, and it is normally distributed with a standard deviation of 0.4 m/s

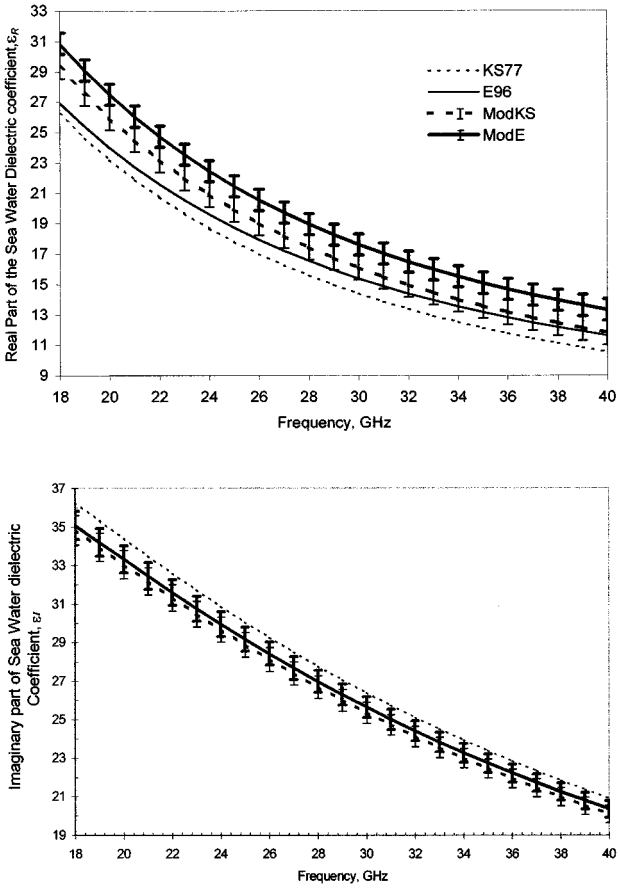


Fig. 3. Nominal and modified ocean dielectric permittivity models KS77 and ModKS (dash lines) and E96 and ModE (solid lines). The plots show the variation in both the real and imaginary parts of the permittivity versus frequency. The error bars denote the standard deviations in the modified models. All plots are for $T_{sea} = 280$ K and $S = 35^0/_{00}$.

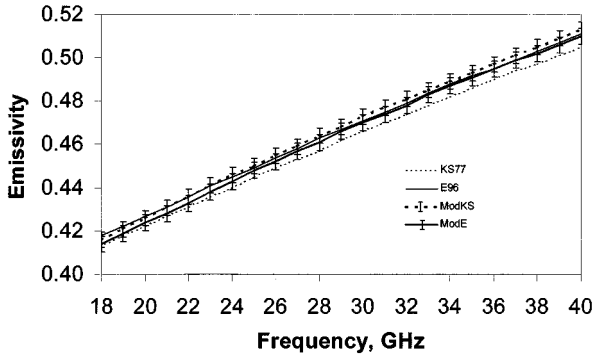


Fig. 4. Nominal and modified specular ocean emissivity models KS77 and Mod KS (dash lines) and E96 and ModE (solid lines) versus frequency. The error bars denote the standard deviations in the modified models. The plot is for $T_{sea} = 280$ K and $S = 35^0/_{00}$.

(see Section III-A). The RMS is also normal, with a standard deviation of 1.4 m/s.

The two parameters $c_R$ and $c_I$ were repeatedly estimated with independent errors added to the data to obtain 1,000 simulated noise realizations. For ModKS, the standard deviations in the $c_R$ and $c_I$ parameters are found to be 0.031 and 0.022, respectively, with a correlation of 0.574. The standard deviations in the $c_R$ and $c_I$ parameters are 0.040 and 0.022, respectively, with a correlation of 0.303 for the modified E96 model. Note that the changes in $\varepsilon_R$ (of 12% and 15%) are therefore statistically significant. The 4% change in $\varepsilon_I$ for KS77, but not the 0.1% change in $\varepsilon_I$ for E96, is significant relative to the $\pm 2.2\%$ error in the change.

The largest sources of error in determining the retrieved parameters were found to be the uncertainties in the salinity and sea surface temperature readings from NODC, followed by TMR instrument calibration errors and then by the spatial and temporal decorrelation uncertainty. Uncertainties in the NODC data added errors of 0.0448 and 0.0081 to $c_R$ and $c_I$, respectively. The error contribution from TMR instrument calibration was found to be 0.0219 and 0.0185, whereas the TMR decorrelation error was 0.0165 and 0.0056 for each of the retrieved parameters. The contribution from the wind was 0.0073 and 0.0022, whereas the RaOb measurements added errors of 0.0012 and 0.0012 to both parameters $c_R$ and $c_I$ respectively.

The effect that the errors in the parameters have on the dielectric model was addressed by a second noise simulation. In this case, 1,000 independent realizations were simulated in which $\varepsilon_R$ and $\varepsilon_I$ were computed for each of the 263 sea states used by the estimation algorithm. At each realization, the two parameters were randomly perturbed according to the statistics given above. The standard deviations of the 1000 realizations is taken as the accuracy of the estimated parameters. The results are plotted versus frequency in Fig. 3. The figure plots a typical value for the permittivity as a solid line and the standard deviation over the 1000 realizations as an error bar. Also shown as solid lines are the unmodified KS77 and E96 models. As seen in the figure, the real part of the ocean dielectric coefficient is increased for both modified models. The imaginary part of modKS is forced down toward the E96 model, and the E96 is only slightly adjusted, showing the superiority of the original E96 over KS77.

The effect that the errors in the modified parameters have on the total ocean emissivity model was addressed by a third noise simulation. Once again, 1,000 independent realizations were simulated, in which the emissivity was computed for each of the 263 sea states used by the estimation algorithm. At each realization, the real and imaginary part parameters were randomly perturbed according to the statistics given above. The standard deviation of the 1000 realizations is taken as the accuracy of the modified specular emissivity. The results are plotted versus frequency in Fig. 4. Again, a typical value for the emissivity is shown as a solid line, the standard deviation over the 1000 realizations is an error bar, and the unmodified models are also shown as solid lines. From the figure at low frequencies, the emissivities according to KS77 and E96 are both modified so as to approach a value in between them and within the error bars of either. At higher frequencies, both modified models still agree with each other and with E96 within their error bars, but KS77 predicts a statistically significant lower emissivity. The average error in the modified emissivity models over the range 18–40 GHz, is found to be 0.0037 and 0.0035, for ModE and ModKS,

respectively. In terms of brightness temperature, this error translates into approximately $0.0037 \times 290$ K or 1.07 K.

## VI. Conclusion

Recent work to determine the sea water dielectric coefficient was based on laboratory measurements of sea water samples from different parts of the ocean. Although these measurements should have rendered a good understanding of the emission from a calm ocean surface, their accuracy in providing values of the ocean still needed to be examined. Our present investigation of the specular sea emission seen from space provides field verification of the sea water specular emissivity over broader regions of the oceans. We investigate and adjust two ocean dielectric models using well calibrated radiometer data from the TOPEX/Poseidon satellite mission, paying particular attention to reducing the frequency dependence of the model and the overall bias of the estimated brightness. In addition, we evaluate the performance of several models for their dependence on salinity and sea temperature.

The modified models exhibit significant improvements in the estimate of $T_B$. Of the two modified models, ModE exhibits superior overall performance. It has the lowest bias at both frequencies (0.16 and 0.14 K, respectively). Its frequency dependence was decreased from $-2.3$ to 0.30 K, which is half of that exhibited by ModKS, and which will allow for more reliable extrapolation to higher frequencies. In addition, ModE has the lowest dependence on sea surface temperature and the lowest RMS difference of 2.58 K and 3.52 K for 18 GHz and 37 GHz, respectively. For these reasons, we recommend this model for future remote sensing applications involving microwave emission from the ocean.

## References


[1] P.S. Callahan, C. S. Morris, and S. V. Hsiao, "Comparison of TOPEX/POSEIDON $\sigma_0$ and significant wave height distributions to Geosat," *J. Geophys. Res.*, vol. 99, no. C12, pp. 25 015–25 024, Dec. 1994.

[2] V. J. Cardone, "Specification of the wind distribution in the Marine Boundary Layer for wave forecasting," Ph.D. dissertation, Dept. Meteorol. Oceanog., New York Univ., New York, 1969.

[3] C. Cox and W. Munk, "Some problems in optical oceanography," *J. Mar. Res.*, vol. 14, pp. 63–78, Jan. 1955.

[4] S. L. Cruz Pol, C. S. Ruf, and S. J. Keihm, "Improved 20-32 GHz atmospheric absorption model," *Radio Sci.*, vol. 33, no. Sept.-Oct., pp. 1319–1333, 1998.

[5] E. Dobson, F. Monaldo, J. Goldhirsh, and J. Wilkerson, "Validation of GEOSAT altimeter-derived wind speeds and significant wave heights using buoy data," *J. Geophys. Res.*, vol. 92, no. , pp. 10 719–10 731, 1987.

[6] G. Elgered, "Tropospheric radio path delay from ground-based microwave radiometry," in *Atmospheric Remote Sensing by Microwave Radiometry*, Janssen, Ed. New York: Wiley, 1993, pp. 240–243.

[7] W. J. Ellison, A. Balana, G. Delbos, K. Lamkaouchi, L. Eymard, C. Guillou, and C. Pringent, "Study and measurement of the dielectric properties of sea water," CETP/CNRS, France, ESTEC/Contract 11 197/94/NL/CN, 1996.

[8] J. A. Goff, "Final report of the working subcommittee of the international joint commit on psychrometric data," *Trans. ASME*, vol. 71, pp. 903–913, 1949.

[9] C. Guillou, W. Ellison, L. Eymard, K. Lamkaouchi, C. Prigent, G. Delbos, G. Balana, and S. A. Boukabara, "Impact of new permittivity measurements on sea surface emissivity modeling in microwaves," *Radio Sci.*, vol. 33, no. 3, pp. 649–667, 1998.

[10] J. P. Hollinger, "Passive microwave measurements of sea surface roughness," *IEEE Trans. Geosci. Electron.*, vol. GE-9, pp. 165–196, 1971.

[11] M. A. Janssen, "An introduction to the passive microwave remote sensing of atmospheres," in *Atmospheric Remote Sensing by Microwave Radiometry*, Janssen, Ed. New York: Wiley, 1993, pp. 7–12.

[12] M. A. Janssen, JASON microwave radiometer: Critical design review, Jet Propulsion Lab., Pasadena, CA, internal rep., Jan. 15, 1998.

[13] S. J. Keihm, C. Ruf, V. Zlotnicki, and B. Haines, "TMR drift analysis," *Jet Propulsion Lab.*, internal rep., Oct. 6 1997.

[14] L. A. Klein and C. T. Swift, "An improved model for the dielectric constant of Sea Water at microwave frequencies," *IEEE Trans. Antennas Propagat.*, vol. AP-25, Jan. 1977.

[15] H. J. G. Liebe, G. A. Hufford, and M. G. Cotton, "Propagation modeling of moist air and suspended water/ice particles at frequencies below 1000 GHz," in *Proc. AGARD Conf. 542, Atmospheric Radiation Effects Through Natural and Man-Made Obscurants for Visible to MM-Wave Radiation*, Berlin, Germany, May 1993.

[16] J. Nash, J. B. Elm, and T. J. Oakley, Relative humidity sensor performance observed in recent international radiosonde comparison, in 9th Symp. Meteorological Observations and Instrumentation, American Meteorological Society, Charlotte, NC, pp. 43–44, 1995.

[17] National Oceanographic Data Center (NODC), *Global Ocean Temperature and Salinity Profile CD-ROM's*. Washington, DC: The Center, 1991.

[18] W. Norberg, J. Conaway, D. B. Ross, and T. Wilheit, "Measurements of microwave emission from a foam-covered, wind-driven sea," *J. Atmos. Sci.*, vol. 28, pp. 429–435, 1971.

[19] P. W. Rosenkranz, "Absorption of microwaves by atmospheric gasses," in *Atmospheric Remote Sensing by Microwave Radiometry*, M. Janssen, Ed. New York: Wiley, 1993, ch. 2.

[20] C. S. Ruf, S. J. Keihm, B. Subramanya, and M. A. Janssen, "TOPEX/POSEIDON microwave radiometer performance and in-flight calibration," *J. Geophys. Res.*, vol. 99, no. C12, pp. 24 915–24 926, 1994.

[21] C. S. Ruf, S. J. Keihm, and M. A. Janssen, "TOPEX/POSEIDON Microwave Radiometer (TMR): I. Instrument description and antenna temperature calibration," *IEEE Trans. Geosci. Remote Sensing*, vol. 33, pp. 125–137, Jan. 1995.

[22] B. I. Semyonov, "Approximate computation of scattering of electromagnetic waves by rough surface contours," *Radio Eng. Electron Phys.*, vol. 11, pp. 1179–1187, 1966.

[23] A. Stogryn, "The apparent temperature of the sea at microwave frequencies," *IEEE Trans. Antennas Propagat.*, vol. AP-15, pp. 278–286, 1967.

[24] ——, "Equations for calculating the dielectric constant of saline water," *IEEE Trans. Microwave Theory Tech.*, pp. 733–736, 1971.

[25] ——, "The emissivity of sea foam at microwave frequencies," *J. Geophys. Res.*, pp. 1658–1666, 1972.

[26] J. Stum, "A comparison between TOPEX microwave radiometer, ERS-1 microwave radiometer, and European Center for Medium Range Weather Forecasts derived wet trophospheric corrections," *J. Geophys. Res.*, vol. 99, no. C12, 1994.

[27] F. T. Ulaby, R. K. Moore, and A. K. Fung, *Microwave Remote Sensing: Active and Passive*. Reading, MA: Addison-Wesley, 1981, vol. 1.

[28] C. G. Wade, "An evaluation of problems affecting the measurements of low relative humidity on the United States Radiosonde," *J. Atmos. Ocean. Technol.*, vol. 11, no. 3, pp. 687–700, 1994.

[29] F. J. Wentz, "A two-scale scattering model for foam-free sea microwave brightness temperature," *J. Geophys. Res.*, vol. 80, pp. 3441–3446, 1975.

[30] ——, "Measurements of oceanic wind vector using satellite microwave radiometers," *IEEE Trans. Geosci. Remote Sens.*, vol. GE-30, pp. 960–972, 1992.

[31] T. T. Wilheit, "The effect of wind on the microwave emission from the ocean's surface at 37 GHz," *J. Geophys. Res.*, vol. 84, no. C8, pp. 244–249, 1979.

[32] ——, "A model for the microwave emissivity of the ocean's surface as a function of wind speed," *IEEE Trans. Geosci. Electron*, vol. GE-17, no. 4, pp. 960–972, 1979.

[33] D. L. Witter and D. B. Chelton, "A Geosat altimeter wind speed algorithm and a method for Al timeter wind speed algorithm development," *J. Geophys. Res.*, vol. 96, no. C5, pp. 8853–8860, May 1991.

[34] S. T. Wu and A. K. Fung, "A noncoherent model for microwave emissions and backscattering from the sea surface," *J. Geophys. Res.*, vol. 77, pp. 5917–5929, 1972.

**Sandra L. Cruz-Pol** received the B.S. degree in electrical engineering from the Universidad de Puerto Rico (UPR), the M.S. degree in microwave engineering from the University of Massachusetts, Amherst, and the Ph.D. degree in electrical engineering from the Pennsylvania State University, State College. Her graduate research included the calibration of the Microwave Atmospheric Absorption Model near 22 GHz and the Ocean Emissivity Model for Microwave Brightness Temperatures seen from space over calm ocean utilizing data from the TOPEX/Poseidon Satellite Mission.

Since 1991, she has been a faculty member at UPR, where she is currently an Assistant Professor teaching courses in the area of applied electromagnetics. Her research interests include microwave remote sensing of natural phenomena, modeling of the microwave atmospheric absorption and the microwave sea surface emissivity.

Dr. Cruz-Pol is a member of the Tau Beta Pi and Phi Kappa Phi Honor Societies. She has been recipient of NASA, GEM, NFS-GEE, and GTE Fellowships.

**Christopher S. Ruf** (S'85–M'87–SM'92) received the B.A. degree in physics from Reed College, Portland, OR, in 1982, and the Ph.D. degree in electrical and computer engineering from the University of Massachusetts, Amherst, in 1987.

He was with the Microwave Remote Sensing Laboratory, University of Massachusetts, Amherst, from 1983 to 1988. He then joined the technical staff at NASA's Jet Propulsion Laboratory (JPL), and in 1992, he left JPL to join the faculty of The Pennsylvania State University, University Park as an Associate Professor of Electrical Engineering. His current research activities include participation in the TOPEX/Poseidon, GEOSAT Follow-On, Jason-1, and NPOESS CMIS flight missions, ground-based atmospheric remote sensing using millimeter radars, radiometers, and synthetic aperture interferometric radiometry.

Dr. Ruf received the 1997 GRS-S Transactions Prize Paper Award and the 1999 IEEE Judith A. Resnik Award. He is a member of the AGU and Commission F of URSI. He is the current Editor and past Associate Editor of the *IEEE GRS-S Newsletter*. He is a past Guest Editor and Associate Editor for *Radio Science*. He serves or has served on the Technical Program Committees of IGARSS 1996, 1998, 1999, and 2000, and the μRad'96 Specialist Meeting on Microwave Radiometry.